MATERIALS SCIENCE

Ultralarge elastic deformation of nanoscale diamond

Amit Banerjee,[1,2]* Daniel Bernoulli,[3]* Hongti Zhang,[1,4]* Muk-Fung Yuen,[2,5] Jiabin Liu,[1] Jichen Dong,[6] Feng Ding,[6,7] Jian Lu,[1,4] Ming Dao,[3]† Wenjun Zhang,[2,5]† Yang Lu,[1,2,4]† Subra Suresh[8]†

Diamonds have substantial hardness and durability, but attempting to deform diamonds usually results in brittle fracture. We demonstrate ultralarge, fully reversible elastic deformation of nanoscale (~300 nanometers) single-crystalline and polycrystalline diamond needles. For single-crystalline diamond, the maximum tensile strains (up to 9%) approached the theoretical elastic limit, and the corresponding maximum tensile stress reached ~89 to 98 gigapascals. After combining systematic computational simulations and characterization of pre- and postdeformation structural features, we ascribe the concurrent high strength and large elastic strain to the paucity of defects in the small-volume diamond nanoneedles and to the relatively smooth surfaces compared with those of microscale and larger specimens. The discovery offers the potential for new applications through optimized design of diamond nanostructure, geometry, elastic strains, and physical properties.

Diamond, the hardest natural material, is notably stiff and durable. It is also a member of the class of carbon materials with a multitude of applications in mechanics, biomedicine, electronics, and photonics (*1*–*7*). Controlled introduction of microstructures can further enhance the strength and hardness of diamond (*8*, *9*). However, the mechanical characteristics of diamond are offset by poor deformability and relatively high brittleness (*10*). These limitations of diamond motivated investigations (*11*, *12*) of pathways and mechanisms for inducing appreciable or even ultralarge elastic deformation. Such efforts with diamond and other nominally brittle materials also entail development of new methods for elastic strain engineering (*13*–*15*) whereby engineered band structures and corresponding enhancements in electronic and optical properties (*16*, *17*) can be attained. In this study, we demonstrate the occurrence of large, reversible elastic deformation in nanoscale needles of both single-crystalline and polycrystalline diamond. We investigated key characteristics of this reversible elastic deformation through nanomechanical bending experiments conducted in situ on the diamond nanoneedles inside a scanning electron microscope (SEM). We complemented the experimental studies with detailed computational simulations involving the finite element method (FEM) and molecular dynamics to quantify the local tensile and compressive stress and strain variations and the mechanisms underlying mechanical deformation.

We fabricated nanoscale diamond needles by plasma-induced etching of diamond thin films deposited on Si substrates through bias-assisted chemical vapor deposition (*5*). We controlled the shape, size, crystallinity, and density of the nanoneedles by the appropriate choice of growth and etching parameters during deposition. We etched the single-crystalline diamond nanoneedles from a <111>-oriented diamond film (figs. S1 and S2) (*18*).

We mounted the diamond nanoneedles on the Si substrate inside a SEM nanoindenter system (Fig. 1A) for quantitative in situ nanomechanical characterization (Fig. 1B). The downward motion of the indenter tip generated a sideward displacement from the inclined tip surface, thereby bending the nanoneedle after contact (Fig. 1, B and C). With the use of high-resolution transmission electron microscope (HRTEM) imaging, we found that our needles had a smooth surface and a pristine single-crystalline diamond structure along the <111> growth orientation aligned with the nanoneedle axis (Fig. 1D). The fracture mode, when the nanoneedle was bent to failure, was brittle, in line with expectations (Fig. 1E).

We simulated elastic deformation with a FEM model using the actual indenter tip and geometry for each individual nanoneedle (*18*). In FEM simulations, we invoked analyses of nonlinear elasticity and elastic anisotropy (fig. S3), as well as frictional contact between the indenter tip and the nanoneedle with friction coefficients f between 0.1 and 1.0 (fig. S4). We chose these values on the basis of previous observation (*19*)

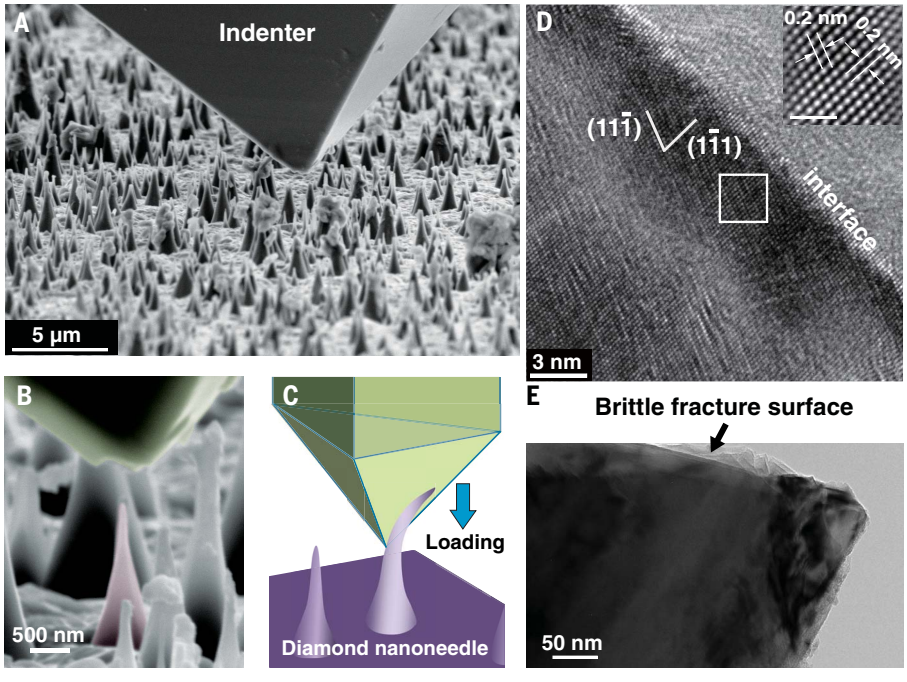

Fig. 1. Experimental setup and nanoneedle characterization. (**A** and **B**) SEM micrographs showing (A) the relative orientation of the diamond nanoneedles with respect to the indenter tip in the experimental configuration and (B) a close-up view of the alignment of the "cube corner" diamond tip of the nanoindenter and a freestanding diamond nanoneedle. (**C**) Schematic representation of the bending deformation of the nanoneedles by the indenter tip's downward motion. (**D** and **E**) TEM micrographs depicting (D) the atomic-scale structure of a pristine diamond nanoneedle sample (inset scale bar, 1 nm) and (E) the smooth fracture surface of a fractured nanoneedle. The inset corresponds to the boxed region in (D).

[1]Department of Mechanical and Biomedical Engineering, City University of Hong Kong, Kowloon, Hong Kong, China. [2]Centre of Super-Diamond and Advanced Films (COSDAF), City University of Hong Kong, Kowloon, Hong Kong, China. [3]Department of Materials Science and Engineering, Massachusetts Institute of Technology, Cambridge, MA 02139, USA. [4]Centre for Advanced Structural Materials, Shenzhen Research Institute of City University of Hong Kong, Shenzhen 518057, China. [5]Department of Materials Science and Engineering, City University of Hong Kong, Kowloon, Hong Kong, China. [6]Center for Multidimensional Carbon Materials, Institute for Basic Science (IBS), Ulsan 44919, Republic of Korea. [7]Department of Materials Science and Engineering, Ulsan National Institute of Science and Technology (UNIST), Ulsan 44919, Republic of Korea. [8]Nanyang Technological University, Singapore 639798, Republic of Singapore.
*These authors contributed equally to this work.
†Corresponding author. Email: mingdao@mit.edu (M.D.); apwjzh@cityu.edu.hk (W.Z.); yanglu@cityu.edu.hk (Y.L.); ssuresh@ntu.edu.sg (S.S.)

that the friction coefficient for diamond on diamond in low-pressure environments, such as the one existing inside the electron microscope, can be much larger than that measured in ambient air.

We found instantaneous full recovery of the nanoneedles to their original, undeformed shape (Fig. 2) when we retracted the nanoindenter tip before the onset of catastrophic fracture. An example of this process is shown in Fig. 2, which presents typical results for a single-crystalline diamond nanoneedle subjected to bending (Fig. 2A, A1 to A4, and movie S1). The maximum horizontal deflection (δ) of the needle tip in Fig. 2A was 442 nm (~19% of the needle's length) at a maximum indentation displacement of 700 nm.

We conducted experiments with larger indentation displacements (Fig. 2B, B1 to B3, and movie S2). We observed δ of 464 nm (~20% of the needle's length) (Fig. 2B, B1) at a maximum indentation displacement of 734 nm just before catastrophic fracture (Fig. 2B, B2 and B3). The needle in Fig. 2 had the largest amount of elastic bending. The smooth fracture surface (highlighted in red in Fig. 2B) indicates that catastrophic failure of the nanoneedle occurred immediately after elastic deformation by atomic separation along preferred crystallographic planes. We confirmed this assessment with ex situ TEM observation of the fractured nanoneedle (Fig. 1E), which showed that the fracture surface was oriented at ~70° with respect to the basal plane. This measurement matches closely with the angle between two {111} planes that are known to be the dominant shear surfaces in single-crystalline diamond (*20*). We found a close overlap between the loading portion of the force-versus-displacement curve (blue curve in Fig. 2C) for the elastic deformation illustrated in Fig. 2A and the subsequent reloading portion of that curve (the portion after complete unloading) for the same nanoneedle (red curve in Fig. 2C) loaded to final fracture as depicted in Fig. 2B. These results indicate fully recoverable elastic deformation during repeat experiments. The hysteresis exhibited by the fully reversible elastic loading-unloading curve (Fig. 2C) arises from frictional contact between the indenter tip and the nanoneedle.

Figure 2 shows FEM simulation of deformed geometry, along with predictions of the maximum principal strain distribution (Fig. 2D) for the monocrystalline nanoneedle just before the onset of catastrophic fracture for the experimental conditions (Fig. 2B, B1). We assumed f of 1.0 for contact between the indenter tip and the needle and Young's modulus E of 1100 GPa for diamond (*18*). We estimated a local maximum tensile stress of ~98 GPa from the simulation, corresponding to a local (tensile) maximum principal strain of 8.88% on the tension side of the bent needle at the maximum indentation displacement of 734 nm. Our simulation of the bent shape of the nanoneedle (Fig. 2D) matches the shape we observed experimentally (B1 in Fig. 2B). Our simulated δ of 478 nm matches well with our experimental observation of 464 nm. We also carried out FEM simulation with smaller friction coefficients, where the local (tensile) maximum principal strain was 8.92% for f = 0.1 and 8.93% for f = 0. These simulations confirm that the maximum strain is determined mainly by the extent of bending and that it is not sensitive to the friction coefficient (fig. S4) or the diamond elastic modulus (table S1). The estimated maximum local tensile stress, however, does depend on the assumed elastic modulus in FEM simulations and would be 89 to 98 GPa (table S1) for the case in Fig. 2B, corresponding to the commonly observed diamond modulus of 1000 to 1100 GPa (*10*).

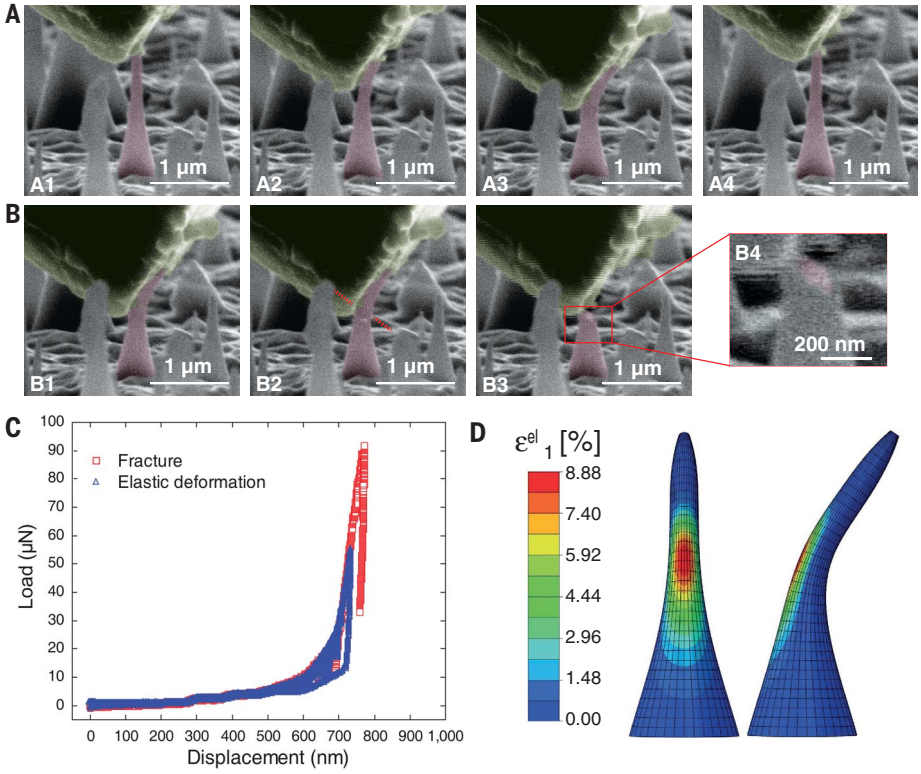

Fig. 2. Ultralarge elastic deformation achieved in a single-crystalline nanoneedle. (**A**) SEM micrographs of the bending deformation of a nanoneedle during loading and subsequent full recovery after unloading. (**B**) Subsequent rerun with the same nanoneedle and larger deformation to the point of catastrophic fracture (B2 shows the maximum deformation immediately before the fracture, B3 shows a moment after the fracture has occurred, and B4 provides a close-up view of the smooth fracture surface, with a characteristic angular orientation). (**C**) Load-displacement curves measured by pushing the nanoindenter tip onto the nanoneedle for the fully reversible elastic deformation (blue curve) and the final fracture run (red curve). (**D**) FEM simulation of the bending process, reproducing the shape of the bending and showing the local elastic (tensile) maximum principal strain (ε^{el}_1) distribution for the nanoneedle, with the frictional coefficient taken as f = 1.0.

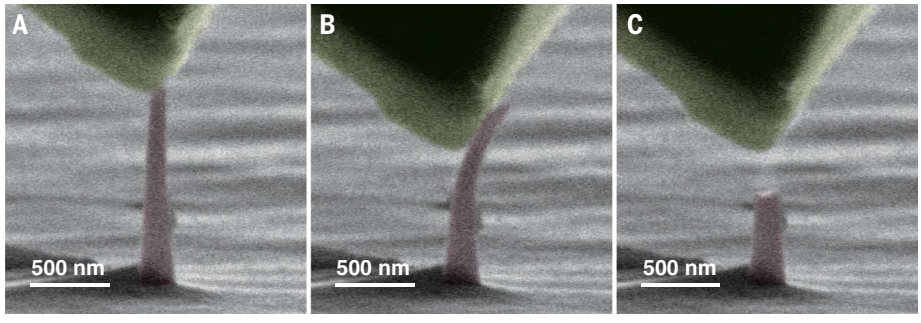

Fig. 3. Large elastic deformation achieved in a polycrystalline nanoneedle. (**A** to **C**) SEM image sequence of bending deformation of a typical polycrystalline nanoneedle, where (B) shows the maximum deformation before fracture and (C) shows the nanoneedle immediately after fracture has occurred.

We carried out five repeat experiments on five different single-crystalline diamond nanoneedles. We observed large, reversible, elastic deformation in each case. We loaded three out of five nanoneedles to the point of fracture. The peak local maximum principal strain from FEM simulation ranged from ~9 to 4% (Fig. 2B, fig. S5, and movie

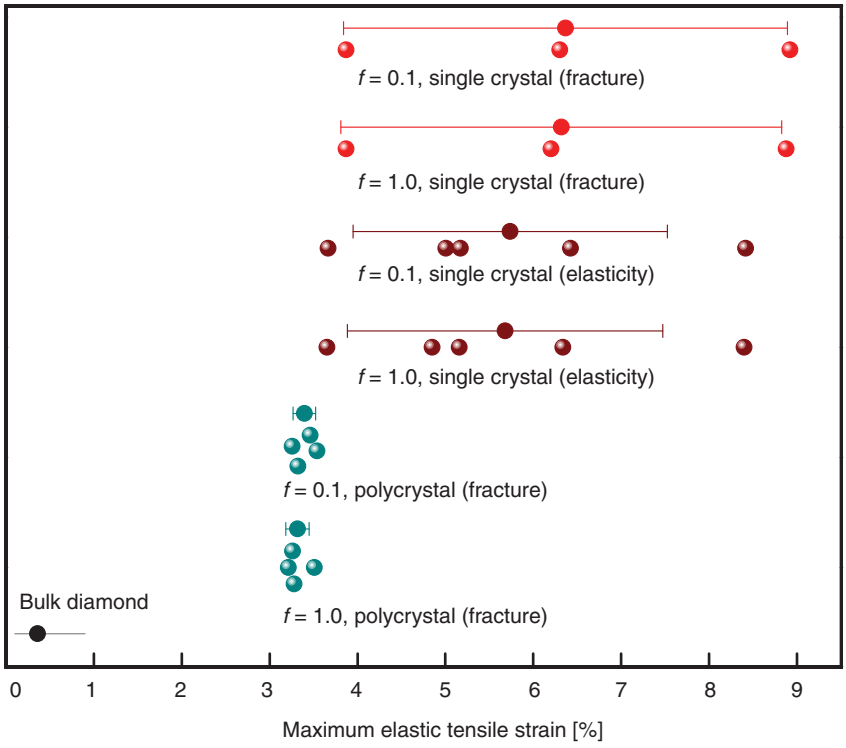

Fig. 4. Summary of the maximum elastic tensile strains. The results were extracted by FEM analysis on the basis of nanoneedle bending experiments, assuming friction coefficient f = 1.0 or 0.1. The data from eight experiments with five different single-crystalline samples (final fracture and fully reversible runs are shown by red and brown data points, respectively) and four experiments with four different polycrystalline samples (shown by cyan circles) are presented. These large elastic strains are much higher than the previously reported bulk diamond elastic limit (shown by the black data point) (*21*).

S3) for single-crystal samples loaded to the point of fracture. We also carried out additional experiments by bending the single-crystalline needles with sideward indenter tip movement, again achieving high tensile strains (fig. S6 and movie S4) (*18*).

We performed similar in situ bending experiments on polycrystalline diamond nanoneedles (Fig. 3, figs. S7 and S8, and movies S5 and S6). Unlike those in single-crystalline needles, fracture surfaces in polycrystalline needles were nearly parallel to the substrate (Fig. 3C). The local (tensile) maximum principal strain from FEM simulation was between 3.51% (f = 1.0) and 3.54% (f = 0.1) for the polycrystalline needle, which is approximately one-half the average for single crystals (*18*). The single-crystalline diamond nanoneedles generally achieved a much higher local maximum tensile strain than the polycrystalline ones (Fig. 4). For the single-crystalline nanoneedles, we achieved a mean maximum tensile strain of ~6% and a peak maximum tensile strain of ~9%. For the polycrystalline nanoneedles, the mean maximum tensile strain was ~3.3% and the peak maximum tensile strain was 3.5%. These large elastic strains are much higher than the previously reported bulk diamond elastic limit (*21*).

We conducted a hybrid density functional theory–molecular dynamics calculation (fig. S9, A and B), which showed the ideal maximum tensile strain to be ~13% along the <111> direction, with C–C bond fracture beyond this critical strain (*18*). We ascribed the ultrahigh elasticity of the diamond nanoneedles (~9% of the maximum tensile strain) to the paucity of internal defects and the relatively smooth surface (Fig. 1D). The nanoscale dimensions of the diamond needles (see the pristine single crystal in Fig. 1D) help avoid internal defects and improve smoothness, compared with that of microscale and macroscale specimens. These factors render it more difficult to initiate a surface crack at these heterogeneous nucleation sites (*18*).

In addition to the maximum elastic tensile strains shown in Fig. 4, we extracted the corresponding maximum elastic compressive strains (up to ~10% or more) observed on the compression side of each sample (fig. S10) (*18*). The related local maximum compressive stress reaches ~100 to 110 GPa (with a diamond modulus of 1000 to 1100 GPa), comparable to the values reported in (*22*).

We showed that single-crystalline diamond nanoneedles are capable of undergoing large elastic bending deformation approaching the theoretical elastic strain limit of diamond, with the corresponding local stress approaching the ideal strength. We demonstrated experimentally that single-crystalline needles are simultaneously ultrastrong and susceptible to large elastic deformation, with fully reversible mechanical deformability of up to a maximum of 9% of elastic tensile strain. Shrinking the diamond needles offers another pathway for achieving elastic strain engineering (*13*–*17*) of diamond. With a focus on physical properties, such as deformation, lattice strains, and band structure, diamond could be engineered to enhance the structural and functional performance of small-volume structures. Large elastic deformation in nanoscale diamond needles could lead to performance enhancements in applications involving bioimaging and biosensing (*7*), strain-mediated nanomechanical resonators (*23*), drug delivery (*7*), data storage (*24*), and optomechanical devices (*25*), as well as ultrastrength nanostructures (*13*, *14*).

REFERENCES AND NOTES

1. A. L. Robinson, *Science* **234**, 1074–1076 (1986).
2. W. Zhu, G. P. Kochanski, S. Jin, *Science* **282**, 1471–1473 (1998).
3. I. Aharonovich, A. D. Greentree, S. Prawer, *Nat. Photonics* **5**, 397–405 (2011).
4. V. N. Mochalin, O. Shenderova, D. Ho, Y. Gogotsi, *Nat. Nanotechnol.* **7**, 11–23 (2011).
5. X. Zhu *et al.*, *Adv. Healthc. Mater.* **5**, 1157–1168 (2016).
6. Y. Wang *et al.*, *Nat. Commun.* **5**, 4466 (2014).
7. X. Chen, W. Zhang, *Chem. Soc. Rev.* **46**, 734–760 (2017).
8. K. Tanigaki *et al.*, *Nat. Commun.* **4**, 2343 (2013).
9. Q. Huang *et al.*, *Nature* **510**, 250–253 (2014).
10. J. E. Field, *The Properties of Natural and Synthetic Diamond* (Academic Press, 1992).
11. M. Seal, *Nature* **182**, 1264–1267 (1958).
12. R. J. Hemley, H. Mao, G. Shen, J. Badro, P. Gillet, M. Hanfland, D. Häusermann, *Science* **276**, 1242–1245 (1997).
13. T. Zhu, J. Li, *Prog. Mater. Sci.* **55**, 710–757 (2010).
14. J. Li, Z. Shan, E. Ma, *MRS Bull.* **39**, 108–114 (2014).
15. D. Yu, J. Feng, J. Hone, *MRS Bull.* **39**, 157–162 (2014).
16. V. M. Pereira, A. H. Castro Neto, *Phys. Rev. Lett.* **103**, 046801 (2009).
17. H. Watanabe, C. E. Nebel, S. Shikata, *Science* **324**, 1425–1428 (2009).
18. Materials and methods are available as supplementary materials.
19. Z. Feng, Y. Tzeng, J. E. Field, *J. Phys. D Appl. Phys.* **25**, 1418–1424 (1992).
20. R. H. Telling, C. J. Pickard, M. C. Payne, J. E. Field, *Phys. Rev. Lett.* **84**, 5160–5163 (2000).
21. J. E. Field, *Rep. Prog. Phys.* **75**, 126505 (2012).
22. J. M. Wheeler *et al.*, *Nano Lett.* **16**, 812–816 (2016).
23. P. Ovartchaiyapong, K. W. Lee, B. A. Myers, A. C. B. Jayich, *Nat. Commun.* **5**, 4429 (2014).
24. S. Dhomkar, J. Henshaw, H. Jayakumar, C. A. Meriles, *Sci. Adv.* **2**, e1600911 (2016).
25. B. Khanaliloo *et al.*, *Phys. Rev. X* **5**, 041051 (2015).

ACKNOWLEDGMENTS

Funding: The work was supported by the Research Grants Council of the Hong Kong Special Administrative Region, China, under the projects CityU11216515 and CityU11207416 and by the National Natural Science Foundation of China under the project 51301147. W.Z. acknowledges the National Natural Science Foundation of China (grants 51372213 and 51672230). M.D. and D.B. acknowledge support by the Singapore-MIT Alliance for Research and Technology (SMART). J. Lu acknowledges support by the Shenzhen Science, Technology and Innovation Commission under grant JSGG20141020103826038. D.B. acknowledges support by the Advanced Postdoc Mobility fellowship from the Swiss National Science Foundation under grant P300P2_167604. J.D. and F.D. acknowledge the support of the IBS of South Korea (grant IBS-R019-D1). A.B. acknowledges a CityU International Transition Team–Graduate Teaching Assistants scheme (ITT-GTA) postdoctoral fellowship. S.S. thanks Nanyang Technological University, Singapore, for support through the Distinguished University Professorship. **Author contributions:** Y.L., W.Z., M.D., and S.S. supervised the research. Y.L. designed the experiments. A.B., D.B., H.Z., M.-F.Y., J. Liu, J.D., and F.D. performed the research. A.B., D.B., H.Z., J. Lu, M.D., W.Z., Y.L., and S.S. analyzed the data and discussed the results. A.B., D.B., H.Z., M.D., W.Z., Y.L., and S.S. wrote the manuscript. All authors reviewed and contributed to the final manuscript. **Competing interests:** None declared. **Data and materials availability:** All data are reported in the paper or the supplementary materials.

SUPPLEMENTARY MATERIALS

www.sciencemag.org/content/360/6386/300/suppl/DC1
Materials and Methods
Supplementary Text
Figs. S1 to S10
Table S1
References (*26*–*45*)
Movies S1 to S6

6 November 2017; accepted 5 March 2018
10.1126/science.aar4165